

RESEARCH

Open Access



# MALDI mass spectrometry imaging (MSI) reveals molecular and structural heterogeneity of amyloid- $\beta$ in sporadic Alzheimer's disease and Down syndrome

Karolina Minta<sup>1,2,3</sup>, Linda Söderberg<sup>1</sup>, Eleni Gkanatsiou<sup>1</sup>, Malin Johannesson<sup>1</sup>, Christer Möller<sup>1</sup>, My Björklund<sup>1</sup>, Gunilla Osswald<sup>1</sup>, Lars Lannfelt<sup>1</sup>, Susanne Fabre<sup>1</sup> and Wojciech Michno<sup>2,3\*</sup>

## Abstract

Alzheimer's disease (AD) and Down syndrome (DS) are both characterized by early accumulation of amyloid- $\beta$  (A $\beta$ ), but the underlying mechanisms differ. In DS, lifelong overproduction of A $\beta$  due to triplication of the APP gene drives pathology, whereas in sporadic AD (sAD) impaired clearance and altered processing are considered to be major contributors to A $\beta$  pathology. Despite these shared hallmarks, it remains unclear whether the molecular composition of plaques, such as A $\beta$  isoform distribution and post-translational modifications, is truly comparable between the two conditions. Most published studies rely on bulk tissue or antibody-based methods, which average across plaques and overlook truncated or modified A $\beta$  isoforms, such as N-terminally or C-terminally truncated forms or pyroglutamate-modified species. Here, we applied a reflector-mode matrix-assisted laser desorption/ionization mass spectrometry imaging (MALDI-MSI) approach, integrated with histology and immunoassay, to characterize A $\beta$  pathology in postmortem brain tissue from DS, sAD, and non-demented control patients at single-plaque resolution. We demonstrate that A $\beta$  plaques and neurofibrillary tangles are significantly larger in DS than in sAD, consistent with more aggressive disease progression. Molecular profiling revealed distinct peptide repertoires between the diseases. DS plaques contained nearly twice as many N-terminally truncated A $\beta$  peptides as sAD, with proportionally similar contributions from A $\beta$ <sub>x-40</sub> and A $\beta$ <sub>x-42</sub>, and uniquely harbored A $\beta$ <sub>2-42</sub>, A $\beta$ <sub>pE3-42</sub>, A $\beta$ <sub>3-40</sub>, A $\beta$ <sub>4-42</sub>, A $\beta$ <sub>8-42</sub>, and A $\beta$ <sub>pE11-40/42</sub>. In contrast, sAD plaques were dominated by truncated A $\beta$ <sub>40</sub> while A $\beta$ <sub>42</sub> remained largely full-length, and only sAD contained bi-terminally truncated isoforms such as A $\beta$ <sub>2-37</sub>, A $\beta$ <sub>2-39</sub>, and A $\beta$ <sub>9-38</sub>. Overall, inter-peptide correlations between the relative abundances of all A $\beta$  peptides as performed across individual plaques were significantly stronger in sAD than in DS, indicating that peptide levels co-vary more consistently within sAD plaques. Collectively, these findings indicate that A $\beta$  plaques in DS and sAD differ in their molecular composition and peptide profiles. Beyond providing mechanistic insight, these findings highlight the need to tailor A $\beta$ -targeting therapies to disease-specific peptide signatures, particularly for individuals with DS, who are at exceptionally high risk of dementia and have been underrepresented in clinical research.

\*Correspondence:  
Wojciech Michno  
wojciech.michno@scilifelab.uu.se

Full list of author information is available at the end of the article



© The Author(s) 2026. **Open Access** This article is licensed under a Creative Commons Attribution 4.0 International License, which permits use, sharing, adaptation, distribution and reproduction in any medium or format, as long as you give appropriate credit to the original author(s) and the source, provide a link to the Creative Commons licence, and indicate if changes were made. The images or other third party material in this article are included in the article's Creative Commons licence, unless indicated otherwise in a credit line to the material. If material is not included in the article's Creative Commons licence and your intended use is not permitted by statutory regulation or exceeds the permitted use, you will need to obtain permission directly from the copyright holder. To view a copy of this licence, visit <http://creativecommons.org/licenses/by/4.0/>.

**Keywords** Alzheimer's disease, Amyloid  $\beta$ , Down syndrome, Matrix-assisted laser desorption/ionization-mass spectrometry imaging

## Introduction

Alzheimer's disease (AD), a progressive neurodegenerative disorder, and Down syndrome (DS), a genetic condition caused by trisomy 21, both feature early accumulation of amyloid- $\beta$  (A $\beta$ ) [1]. Although the two disorders share this hallmark pathology, they arise from distinct mechanisms. In AD, impaired A $\beta$  clearance and altered processing occur [2], whereas in DS, lifelong A $\beta$  overproduction results from the triplication of the amyloid precursor protein (APP) gene [3]. By midlife, virtually all individuals with DS harbor A $\beta$  plaques, and most develop dementia a decade or two earlier than those with sporadic AD (sAD) [4]. This predictable and aggressive trajectory makes DS a uniquely informative clinical population for understanding the biology of A $\beta$  deposition. At the same time, individuals with DS remain overlooked in therapeutic development, despite being among those most affected by A $\beta$  pathology. The recent approval of A $\beta$ -targeting antibodies highlights this gap: while such therapies are being evaluated for sporadic and familial AD, their efficacy and safety in DS, who exhibit distinct A $\beta$  peptide profiles, remain almost entirely unexplored [5, 6]. A deeper molecular understanding of A $\beta$  pathology in DS is therefore urgently needed, both to illuminate disease-specific mechanisms, and to ensure that individuals with DS are not excluded from the benefits of emerging treatments.

A $\beta$  peptides are generated by sequential proteolysis of APP, yielding a spectrum of isoforms that differ in length and aggregation properties [7]. Among these, A $\beta$ 1-40 and A $\beta$ 1-42 are the most abundant, with A $\beta$ 42 being particularly prone to oligomerization and protofibril formation [8]. In addition to these full-length forms, truncated variants arise through further processing by proteases such as BACE1 (which acts both as a  $\beta$ -secretase initiating A $\beta$  production and as an A $\beta$ -degrading enzyme (ADE) generating N-terminally truncated species such as A $\beta$ pE3-42 and A $\beta$ 4-42), BACE2, aminopeptidases, and  $\gamma$ -secretase trimming, as well as through the activity of other ADEs, including neprilysin and insulin-degrading enzyme (IDE). These enzymes contribute to the heterogeneity of A $\beta$  peptides observed in the human brain by generating N-terminal (e.g., A $\beta$ 3-x, A $\beta$ 11-x) and C-terminal (e.g., A $\beta$ 1-37, A $\beta$ 1-38, A $\beta$ 1-39) truncated species, which can profoundly alter aggregation kinetics, seeding efficiency, and toxicity [9–12]. Soluble A $\beta$  oligomers and protofibrils are thought to be the most neurotoxic forms, and thus primary targets for therapeutic intervention [13]. The balance of full-length versus truncated peptides

may therefore critically shape disease trajectories in AD and DS.

Previous comparative studies of DS and AD have reported both similarities and differences in the composition of A $\beta$  pathology. PET imaging and bulk analyses of homogenized brain tissue have shown comparable rates of accumulation and overlapping peptide profiles [12, 14–19], whereas other work suggests earlier deposition and higher absolute levels of A $\beta$ 40 and A $\beta$ 42 in DS [20]. A major limitation of these approaches, however, is that they average across many plaques and often rely on antibody-based detection, capturing only selected epitopes. As a result, they obscure the molecular heterogeneity of individual lesions and overlook truncated or modified isoforms not recognized by available antibodies.

It is increasingly recognized that A $\beta$  plaques are not chemically uniform but rather mosaics of distinct A $\beta$  isoforms arranged in spatially distinct microdomains, with compositions and post-translational modifications that vary with plaque type, maturation state, and disease progression [21]. These patterns likely reflect specific aggregation pathways and proteolytic environments and resolving them at the level of single plaques is critical for understanding disease-specific mechanisms. Matrix-assisted laser desorption/ionization mass spectrometry imaging (MALDI-MSI) provides precisely this capability, enabling direct, label-free detection of peptides within intact tissue sections while preserving spatial context. Prior work in AD done by us, and others, has shown that MALDI-MSI can resolve heterogeneous A $\beta$  peptide repertoires across plaques [22–30], but this approach has not yet been systematically applied to DS.

The APOE genotype is a major genetic risk factor for sAD, influencing A $\beta$  aggregation, deposition, and clearance. Specifically, the APOE  $\epsilon$ 4 allele is associated with increased A $\beta$  plaque burden and accelerated aggregation compared to  $\epsilon$ 3 and  $\epsilon$ 2 alleles [31]. The isoform-dependent pattern of A $\beta$  accumulation is primarily modulated via differential regulation of A $\beta$  clearance from the brain [32].

In this study, we employed a newly optimized reflector mode MALDI-MSI approach, combined with fluorescence histology and immunoassay, to characterize the composition and spatial organization of A $\beta$  peptides in postmortem brain tissue from individuals with DS, sAD, and age-matched non-demented controls. By interrogating A $\beta$  pathology at the level of individual plaques, we aimed to uncover disease-specific peptide signatures and aggregation patterns that would be masked in bulk methods. Our findings reveal marked differences in the

truncation profiles, spatial organization, and peptide co-localization of A $\beta$  in DS and sAD, highlighting distinct disease-specific mechanisms underlying A $\beta$  generation, processing, aggregation, and plaque deposition in each condition. These insights are not only mechanistically informative but also clinically relevant, suggesting that therapeutic strategies targeting A $\beta$  may need to be tailored to the molecular signatures that distinguish DS from sAD.

## Materials and methods

### Patient selection and characteristics

Post-mortem human brain tissue was obtained from the Netherlands Brain Bank (NBB), Netherlands Institute for Neuroscience, Amsterdam (see Table 1 for demographic characteristics). Brain tissues from sAD (n=3) and DS (n=3) patients were selected to be matched based on Braak stage ( $\geq 5$ ), APOE genotype ( $\epsilon 3/\epsilon 3$ ), and gender (1:2, male:female). Only APOE  $\epsilon 3/\epsilon 3$  individuals were included to minimize confounding effects of the  $\epsilon 4$  allele, which can directly influence amyloid deposition, and to allow a clearer assessment of A $\beta$  processing and pathology development independent of APOE genotype. A non-demented control group (n=3) with low pathology (Braak stage  $\leq 2$ ) was also included. All samples were obtained from the same brain region—the frontal gyrus. All material has been collected from donors whose written informed consent for brain autopsy and the use of the material and clinical information for research purposes has been obtained by the NBB. The informed consent form of the NBB meets all current legal and ethical requirements for brain autopsy, tissue storage and use of tissue and clinical data for scientific research worldwide. The study followed the Helsinki Declaration and was approved by the Swedish Ethical Review Authority (2020-00527 and 2021-00965).

### APOE genotyping

APOE genotyping for non-demented control samples was either provided by the NBB or determined using a commercial qPCR kit (Creative Biogene, Shirley, NY, USA). Genomic DNA was extracted prior to analysis

using the QIAwave DNA Blood & Tissue Kit (Qiagen, Hilden, Germany).

### Chemicals and reagents

All chemicals for matrix and solvent preparation were pro-analysis grade and obtained from Sigma-Aldrich/Merck (St. Louis, MO, USA) unless otherwise specified. Deionized water was obtained by a Milli-Q purification system (Millipore Corporation, Merck, Darmstadt, Germany).

### Tissue sectioning

For correlative MSI/GeoMx analyses, sagittal cryosections (10  $\mu$ m) were prepared from fresh-frozen brain tissue using a cryostat microtome (Leica CM1520, Leica Biosystems, Nussloch, Germany) operated at  $-18$  °C. Sections designated for GeoMx DSP were thaw-mounted onto SuperFrost Plus slides, while adjacent sections were placed on conductive indium tin oxide (ITO)-coated glass slides (Bruker Daltonics, Bremen, Germany) for MALDI-MSI. All specimens were stored at  $-80$  °C until use.

### Amyloid staining and fluorescence imaging (FI)

For plaque visualization, sections were fixed sequentially in 95% ethanol (1 min), 50% ethanol in water (30 s), and water (1 min), followed by incubation with the optotracer Amytracker 520 (1:1000 in water; Ebba Biotech AB, Stockholm, Sweden) for 30 min at room temperature in the dark. Sections were rinsed briefly in water, desiccated, and stored at 4 °C until imaging. This LCO staining previously shown to co-localize with A $\beta$  plaque- and tau tangle-specific antibodies [33, 34]. The A $\beta$  plaques were identified based on size, staining positivity, and MSI A $\beta$  signal positivity, and the NFTs were identified based on size, fibrillar, thread-like tangle structure, and staining positivity. Fluorescent imaging was performed on an automated widefield scanner (Axio Scan Z1, Zeiss, Oberkochen, Germany). Large multi-channel z-series tile scans were acquired using a Plan-Apochromat 20 $\times$ /0.8 DIC air objective and an ORCA monochrome camera (Hamamatsu, Shizuoka, Japan). Excitation and emission

**Table 1** Patients' demographics

Diagnostic group	ID	Age	Gender	APOE genotype	Braak stage	Brain region
Down syndrome	DS1	58	F	3/3	VI	Frontal gyrus
	DS2	67	F	3/3	VI	Frontal gyrus
	DS3	64	M	3/3	V	Frontal gyrus
Alzheimer's disease	sAD1	68	F	3/3	V	Frontal gyrus
	sAD2	79	F	3/3	V	Frontal gyrus
	sAD3	56	M	3/3	VI	Frontal gyrus
Non-demented controls	Ctrl1	79	M	3/3	II	Frontal gyrus
	Ctrl2	73	F	4/4	I	Frontal gyrus
	Ctrl3	80	F	3/4	I	Frontal gyrus

filters were matched to the used fluorophores, specifically Alexa Fluor 488 (LED 475 nm, 450–488/504–546 nm). Image processing of the FI images was done in QuPath v0.6.0 [35].

#### Matrix deposition for MALDI-MSI

Fresh-frozen tissue sections mounted on ITO-coated glass slides were fixed in 100% ethanol for 60 s, followed by 70% ethanol for 30 s. Lipids were removed by immersion in Carnoy's solution (ethanol/chloroform/acetic acid, 60/30/10 v/v/v) for 120 s, after which slides were sequentially washed in 100% ethanol (15 s), 0.2% trifluoroacetic acid in water (60 s), and 100% ethanol (15 s). For matrix deposition, a 60 mg/ml mixture of 2, 5-dihydroxybenzoic acid (DHB) and 2-hydroxy-5-methoxybenzoic acid (9:1) was prepared in acetonitrile/ddH<sub>2</sub>O/trifluoroacetic acid (40/60/1 v/v/v) and applied using an M3 + sprayer (HTX Technologies, Carrboro, NC, USA).

#### MALDI-MSI data acquisition and processing

Imaging experiments were performed on a rapiflex MALDI time-of-flight instrument (Bruker Daltonics) operated in reflector positive mode. Data were acquired at 20  $\mu$ m spatial resolution across an m/z range of 2500–5000, with the laser operating at 5 kHz frequency, 52% power, detector gain set to 1.00 at 2280 V, ion source voltage of 19,989 V, reflector voltages of 20,832 V (Reflector 1), 8900 V (Reflector 2), and 8591 V (Reflector 3), and 100 shots accumulated per pixel. Prior to acquisition, the instrument was calibrated with red phosphorus. Tissue areas were selected and monitored using FlexControl 4.2 and FlexImaging 6.0 software (Bruker Daltonics). Data visualization and statistical analyses, including segmentation, were conducted in SCiLS Lab software (v2025a Pro, Bruker Daltonics). In SCiLS, data was baseline subtracted and TIC normalized. Identification of A $\beta$  peptides was done by matching the experimental data against a macro-based curated mass list of all possible human A $\beta$  peptide variants. Peaks corresponding to A $\beta$  species were considered 'detected' if all of the following were true, (i) a clear signal was observed at the expected m/z in the spectrum, (ii) signal could be distinguished from baseline noise (SNR > 3), and (iii) peptide envelope for the given peptide was present. Tissue segmentation was performed in SCiLS Lab using bisecting k-means with a Euclidean distance metric and weak denoising, without spatial smoothing.

#### Alignment of MALDI-MSI and fluorescence microscopy data for plaque analysis

Registration between the two modalities, MSI and fluorescence microscopy, was performed in SCiLS by aligning anatomical landmarks, tissue boundaries, and the A $\beta$  MSI signal. The accuracy of the registration was assessed

visually and is therefore limited to the optical resolution of the images (~10–20  $\mu$ m). This level of precision was sufficient for comparing MSI cluster patterns with LCO fluorescence staining. No additional quantitative assessment of alignment was performed, as this study focused on overall plaque populations rather than intra-plaque features. At 20  $\mu$ m resolution, this approach was adequate to verify the relevant pathological features. When single-plaque analysis was performed, the number of deposits included was limited to that in the subject with the fewest A $\beta$  plaques (effectively rounded up to 300), and the analysis was performed in R (v4.4.1) Studio via random sampling to ensure reproducibility. This was done to avoid over-representation by individual patients.

#### Immunoprecipitation and quantification of soluble A $\beta$ protofibrils

Fresh frozen cerebral tissue (100 mg) was homogenized in (Tris)-buffered saline (TBS), pH 7.6 containing protease and phosphatase inhibitors (cOmplete™ Protease Inhibitor Cocktail and PhosSTOP™ Phosphatase Inhibitor Cocktail, Roche Diagnostics, Mannheim, Germany) in a 1:5 w/v ratio using a Potter-Elvehjem homogenization tubes. After centrifugation (16,000  $\times$  g for 1 h at 4 °C), the supernatant, i.e., TBS fraction, was collected, aliquoted and stored at –80 °C. Immunoprecipitation (IP) was performed using the KingFisher Apex System (Thermo Fisher Scientific, Waltham, MA, USA). TBS extracts were diluted 1:10 in IP buffer (Dulbecco's PBS, 0.1% BSA, 0.5% Tween-20) supplemented with the A $\beta$  protofibril selective antibody mAb158. M-280 Tosyl-activated Dynabeads (Invitrogen, Carlsbad, CA, USA) coupled with mouse-anti-mouse IgG2a (Pharmingen, San Diego, CA, USA) were added and allowed to bind to the mAb158- protofibril complexes. Beads were washed in IP buffer and immunoprecipitated A $\beta$  protofibrils were eluted in 70% formic acid. Extracts were then neutralized 1:30 in a buffer consisting of equal volumes of Diluent 35 (Meso Scale Discovery, Rockville, MD, USA) and 1 M Trizma base and 0.5 M Na<sub>2</sub>HPO<sub>4</sub>. Samples were analyzed using V-PLEX A $\beta$  Peptide Panel (4G8) Kit according to manufacturer's instructions (Meso Scale Discovery). The plate was analyzed using a Mesoscale Sector Imager and levels of A $\beta$ x-38, A $\beta$ x-40 and A $\beta$ x-42 in samples were back calculated against standard curves.

#### Statistical analysis

GraphPad Prism software version 9.5.0 (GraphPad Software, La Jolla, CA, USA) and R studio (v4.4.1) were used for statistical analysis. The normality of the data was assessed using the Shapiro-Wilk test. An unpaired t-test or Mann-Whitney test was used to compare the means or medians, respectively, between two groups. The non-parametric one-way ANOVA on ranks (Kruskal-Wallis)

followed by Dunn's test for multiple comparisons was used when comparing more than two groups. For single plaque correlation analysis, data were log-transformed followed by Pearson correlation.

## Results

### Morphological differences in A $\beta$ and NFT pathology between DS and sAD

A $\beta$  and neurofibrillary tangle (NFT) deposits are hallmark lesions of AD and related neurodegenerative disorders, yet they are far from uniform in structure or appearance. Previous neuropathological studies have shown that both A $\beta$  and NFT aggregates vary in size, density, fibrillar architecture, and regional distribution, not only across AD subtypes but also between distinct proteopathies [36–38]. These variations likely reflect differences in aggregation kinetics, local microenvironments, and upstream genetic drivers. In familial forms of AD, pathogenic variants alter APP processing; in sAD, mechanisms are more heterogeneous and less well characterized. In DS, lifelong APP overexpression is expected to accelerate A $\beta$  accumulation, but whether this also yields distinctive morphological signatures of A $\beta$  has been less clear.

We therefore set out to systematically interrogate lesion morphology and link structural features to underlying chemical phenotypes in DS, sAD, and non-demented control brains. To do so, we combined high-sensitivity amyloid-targeted histology, reflector-mode A $\beta$

peptide analysis, and electrochemiluminescence-based detection of A $\beta$  and tau aggregates using luminescent conjugated oligothiophenes (LCOs) (Fig. 1) [24, 30]. Histological inspection revealed abundant A $\beta$  plaques and NFTs in both sAD and DS (Fig. 2a–b), while tissues from non-demented controls were consistently negative for LCO and A $\beta$  signal in MSI (Fig. 2c, Supplementary Fig. 1) in agreement with Braak staging. For each patient, A $\beta$  plaques and NFTs were manually selected across the entire tissue section. Pathological features were included when their identity and boundaries could be unambiguously confirmed by their characteristic morphology and LCO staining patterns. All included structures met the same morphological inclusion criteria. Quantitative tissue density estimates revealed no significant differences in the number of A $\beta$  plaques or NFTs per unit area between sAD and DS, suggesting comparable overall amyloid load in these groups (Fig. 2d). Next, we inspected the morphology of the aggregates by measuring the surface area of A $\beta$  plaques and NFTs. This unbiased sampling revealed a striking size difference: both A $\beta$  plaques and NFTs were larger in DS than in sAD (Fig. 2e–h). The distribution of individual A $\beta$  plaques in DS patients was much higher than in sAD patients (Fig. 2e,  $p < 0.0001$ ), with the average A $\beta$  plaque size approximately five times larger in DS patients than in sAD (Fig. 2f,  $p = 0.009$ ). The size distribution of tangles between sAD and patients largely overlapped (Fig. 2g,  $p < 0.0001$ ), with the average tangle size being roughly double in DS patients compared

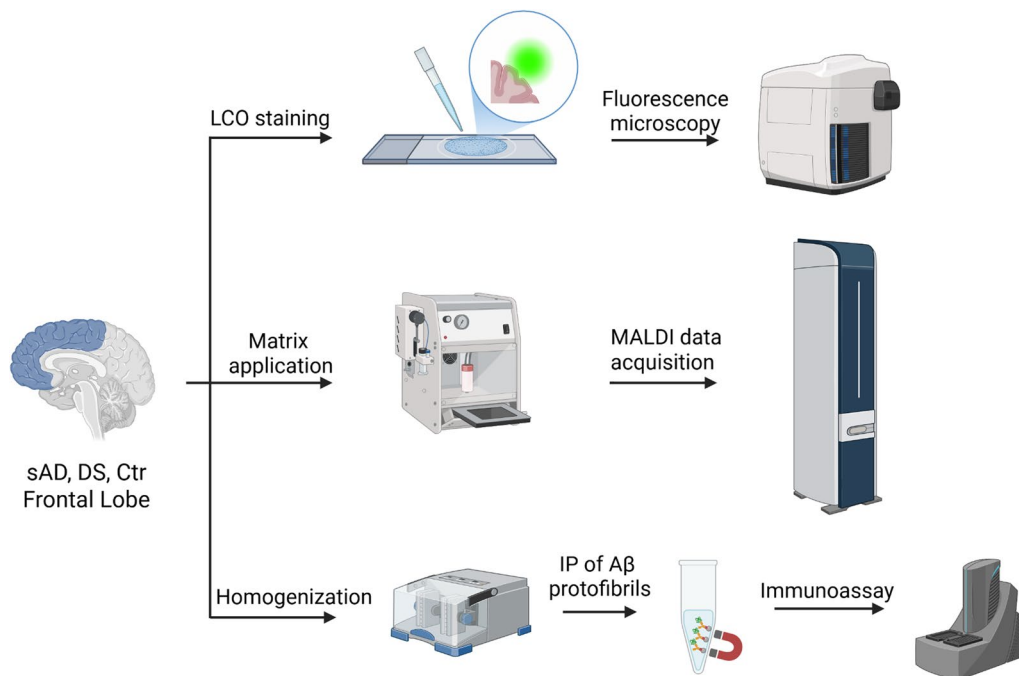


**Fig. 1** Multimodal A $\beta$  analysis workflow. Schematic presentation of the workflow for the fluorescence imaging using luminescent amyloid probes (top), MALDI MSI analysis of A $\beta$  peptide variants (middle) and IP-MSD analysis of A $\beta$  protofibrils (bottom) in human brain tissue from sAD, DS and non-demented control subjects. Created with BioRender.com

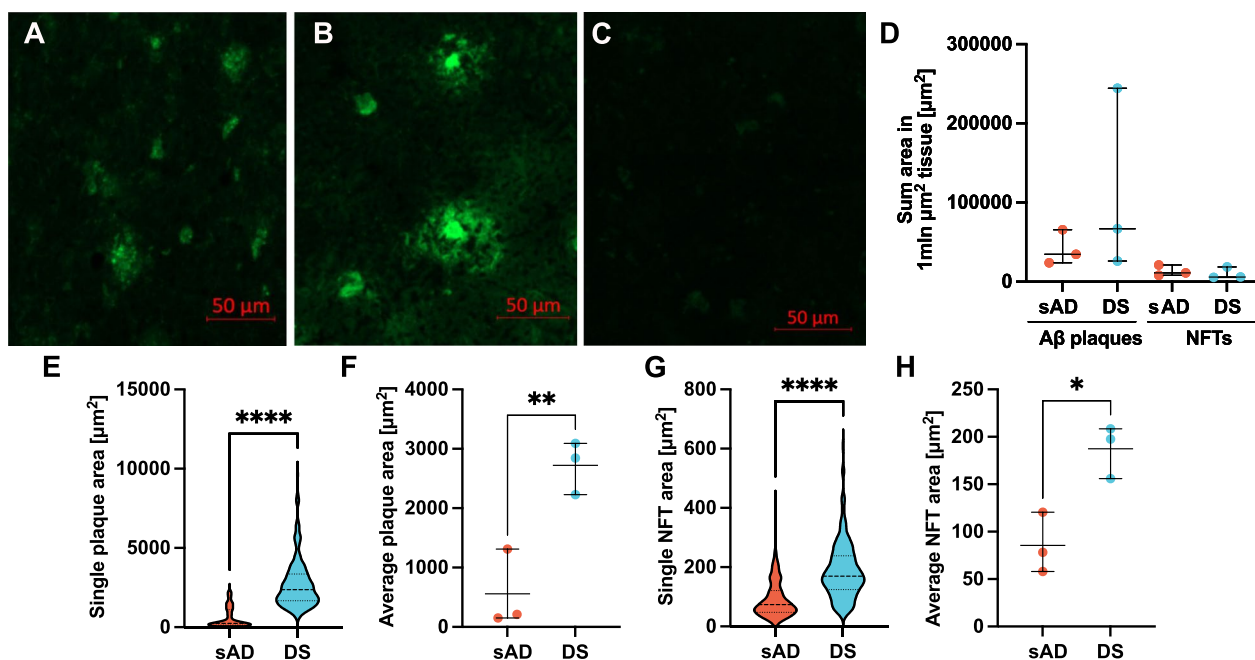


**Fig. 2** Quantification of A $\beta$  plaques and NFTs in sAD and DS. Representative examples of fluorescence imaging of A $\beta$  deposits and NFTs in human brain tissue from sAD (a) DS (b) and non-demented control (c). Comparison of plaque and tangle densities in 1mln  $\mu\text{m}^2$  tissue (d) between sAD (n=3) and DS (n=3) patients. Each symbol represents the total area of all deposits collected per patient. A Kruskal-Wallis test was conducted to compare differences among these groups, followed by Dunn's post hoc test. Comparison of single (e, g) and average (f, h) areas of A $\beta$  plaques (e-f) and NFTs (g-h) in brain tissues. Comparisons between two groups were performed using a Welch's t-test for normally distributed data and a Mann-Whitney test for non-normal data. A  $p$ -value  $\leq 0.05$  was considered statistically significant

with sAD (Fig. 2h,  $p=0.01$ ). Together, these observations suggest that the neuropathological landscape in DS is not merely accelerated but qualitatively distinct, with A $\beta$  deposits co-existing alongside tau pathology.

#### A $\beta$ peptide repertoires revealed by reflector-mode MALDI imaging

Having established that A $\beta$  lesions in DS differ morphologically from those in sAD, we next sought to examine their underlying molecular composition. Characterizing the biochemical heterogeneity of individual A $\beta$  deposits has been challenging, as conventional extraction-based methods require large tissue amounts and often bias detection toward certain aggregation states [39]. MALDI-MSI addresses this challenge by enabling in situ analysis of A $\beta$  pathology without prior extraction, preserving spatial context. However, systematic tissue characterization is still limited by technical constraints. Although linear TOF mode can offer higher intrinsic sensitivity for high-mass ions, in this study, we employed a newly optimized acquisition strategy in reflector mode, which enabled unambiguous assignment of A $\beta$  peptides while maintaining sufficient sensitivity for tissue analysis.

Inspection of average spectra suggested that even on the tissue level the sAD subjects are dominated by more diverse A $\beta$  truncations (Fig. 3a), as represented by the higher diversity of peptides in the lower mass range. At

this stage we also confirmed that our newly developed method was able to separate individual A $\beta$  peptides with overlapping isotope envelope patterns (Fig. 3b). Following data acquisition, the resulting high-dimensional data were interrogated in an unbiased fashion using bisecting k-means clustering. This segmentation approach partitioned the tissue into clusters that corresponded closely to A $\beta$  plaques, and the adjacent parenchyma region. Notably, the segmentation was data-driven and required no prior histological annotation; nevertheless, the overlap with LCO-stained plaques confirmed the accuracy of cluster identification (Fig. 3c-f).

From these plaque-defined clusters, we extracted average ion spectra and peptide distributions, achieving comprehensive coverage of A $\beta$  isoforms in both sAD and DS brains (Fig. 4a, Table 2). Among these, the canonical A $\beta$ 1-40 and A $\beta$ 1-42 peptides were consistently detected across all examined brain sections from both sAD and DS patients. In contrast, the presence and spatial distribution of other A $\beta$  variants varied notably between cases. For instance, while pyroglutamate A $\beta$ 3-40 (A $\beta$ pE3-40) was present in both sAD and DS patients, A $\beta$ pE3-42 was uniquely detected in DS. Similarly, A $\beta$ pE11-40 and A $\beta$ pE11-42 were absent in sAD cases, but present in DS. These findings, delivered from segmentation-based MALDI-MSI analysis, suggest that A $\beta$  plaques in DS harbor a more diverse and broader repertoire of A $\beta$

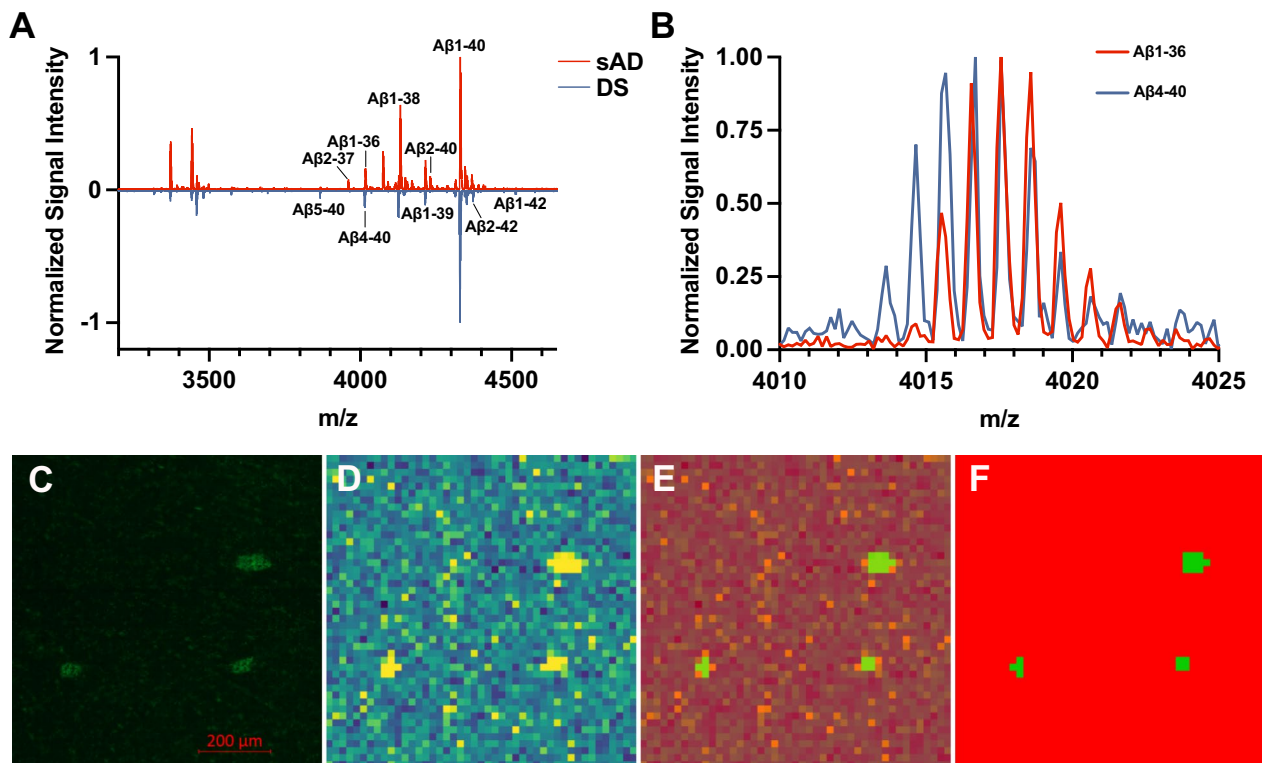


**Fig. 3** Reflector-mode MALDI imaging of A $\beta$  isoforms in DS and sAD brain tissue. Normalized signal intensity spectra from representative sAD and DS patients, with annotation of few major A $\beta$  peptides (a). Separation of overlapping isotope envelope patterns of A $\beta$ 1-36 and A $\beta$ 4-40 achieved using our novel reflector mode MSI approach (b). A representative brain tissue section from a DS patient is shown, illustrating (c) plaque localization via luminescent conjugated oligothiophene (LCO) staining, alongside MALDI-MSI-derived single-ion images of A $\beta$ 1-42 peptide (d), with corresponding 50% (e) and complete (f) segmentation map

isoforms, including A $\beta$ 2-42, A $\beta$ pE3-42, A $\beta$ 3-40, A $\beta$ 4-42, A $\beta$ 8-42, A $\beta$ pE11-40/42, which may be associated with plaque formation earlier as observed in this disorder.

#### Distinct truncation patterns of A $\beta$ isoforms in DS and sAD

We next quantified the distribution of A $\beta$  isoforms across plaque-segmented clusters. A $\beta$  peptides arise from sequential cleavage of APP by  $\beta$ - and  $\gamma$ -secretases, typically producing full-length A $\beta$ 1-40 and A $\beta$ 1-42 as the dominant species. However, additional processing can occur: aminopeptidases can remove residues from the N-terminus (e.g., generating A $\beta$ 2-x, A $\beta$ 3-x, or A $\beta$ 11-x) [40, 41], while carboxypeptidases and alternative  $\gamma$ -secretase trimming can shorten the C-terminus by several residues (e.g., producing A $\beta$ 1-37, A $\beta$ 1-38, or A $\beta$ 1-39) [42]. When both N- and C-terminal processing events occur, bi-terminally truncated species are generated. Such modifications not only diversify the peptide pool but also strongly influence aggregation kinetics and plaque morphology [10]. Therefore, to capture these differences, peptides were grouped into four categories: full-length species, N-terminally truncated (A $\beta$ x-40/x-42), C-terminally truncated, and bi-terminally truncated peptides. Analysis of these peptide fractions across patients

and individual plaques revealed striking differences between conditions (Fig. 4a). In sAD, average plaques contained a two-fold higher proportion of C-terminally truncated peptides than in DS (23.5% vs. 11.1%). On the other hand, the opposite trend was observed for N-terminally truncated species, which contributed roughly a quarter less of all signals (45.9% vs. 75.2%). Surprisingly, pyroglutamate-modified species were significantly less abundant in sAD than in DS, with forms such as A $\beta$ pE3-42 largely absent (Fig. 4b, top). It is possible that this was due to the ApoE  $\epsilon$ 3/ $\epsilon$ 3 genotype of the sAD cases and the fact that these species become more prominent only as the A $\beta$  plaques become older. Conversely, sAD plaques were enriched in bi-terminally truncated species, including A $\beta$ 2-37, A $\beta$ 2-39, and A $\beta$ 9-38 (Fig. 4b, bottom). This points to more complex, multi-step proteolytic cascades in sAD. These observations were confirmed at the single-plaque level, indicating that this separation is not driven by any single patient (Fig. 4c). Further quantification revealed that while in sAD the N-terminal truncations ended largely at amino acid 40 (A $\beta$ x-40), in DS they ended largely at amino acid 42 (A $\beta$ x-42) (Fig. 4d). Together, these results indicate that sAD and DS differ not only in the presence of specific A $\beta$  peptides but also

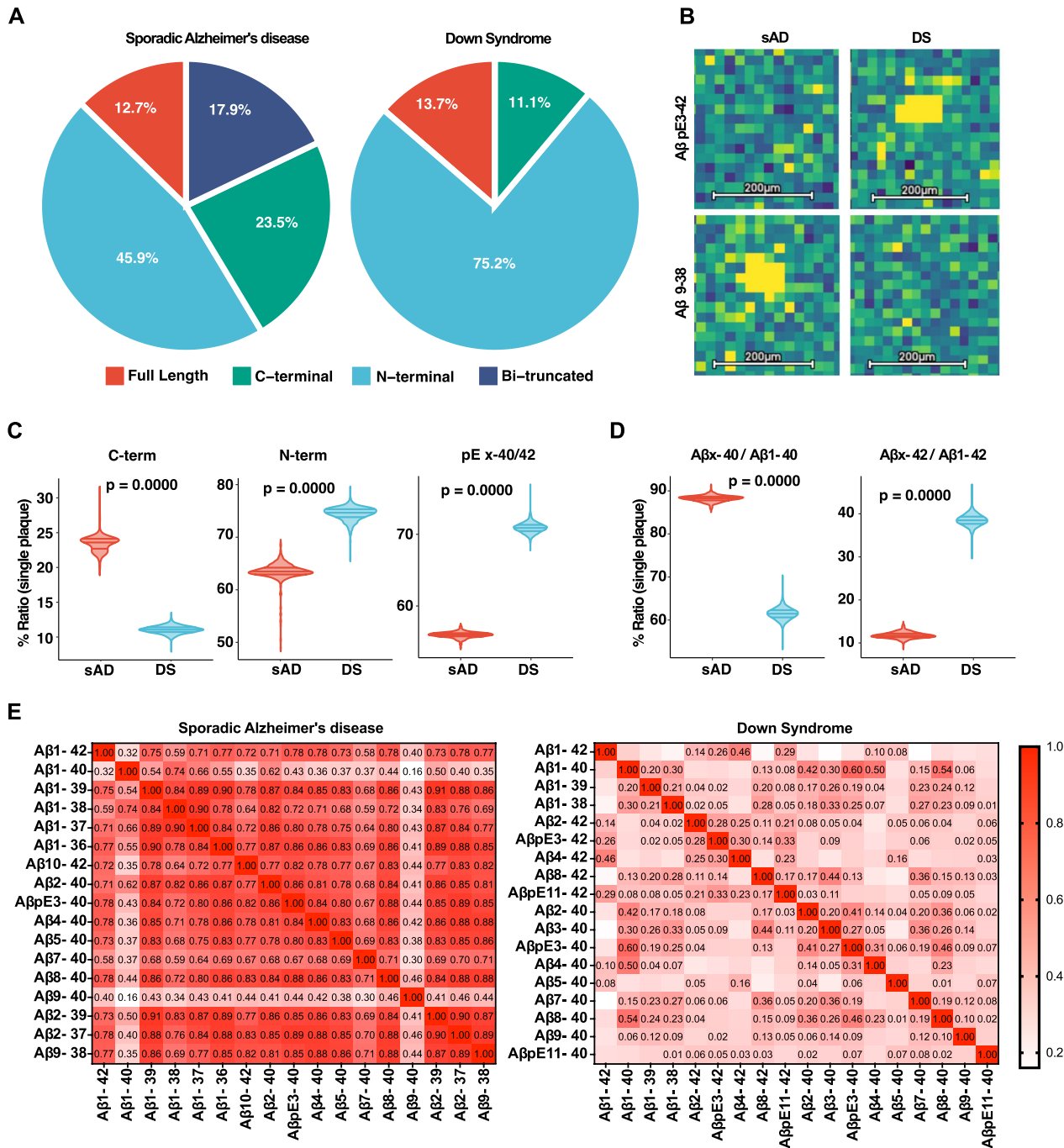


**Fig. 4** Aβ isoform distribution and single-plaque analysis in DS and sAD plaques. Average distribution of Aβ isoforms grouped into full-length, N-terminally truncated (Aβx-40/x-42), C-terminally truncated, and bi-terminally truncated peptides per patient (a). sAD plaques contained a twofold higher proportion of C-terminally truncated peptides compared to DS, while N-terminally truncated species were more abundant in DS. DS plaques were enriched in pyroglutamate-modified species such as AβpE3-42, largely absent in sAD, whereas sAD uniquely contained bi-terminally truncated species including Aβ2-37, Aβ2-39, and Aβ9-38 (b). Single-plaque analysis confirmed these differences are not driven by any individual patient (c). N-terminal truncations in sAD terminate predominantly at amino acid 40 (Aβx-40), whereas in DS predominantly at amino acid 42 (Aβx-42) (d). Pearson correlation matrices of Aβ isoforms within individual plaques reveal stronger inter-peptide co-occurrence in sAD than DS (e)

**Table 2** A $\beta$  peptides list identified in DS and sAD

	Positions	Sequence	sAD	DS
C-truncated A $\beta$	1-42	DAEFRHDSGYEVHHQKLVFFAEDVGSNKGAIIGLMVGGWIA	x	x
	1-40	DAEFRHDSGYEVHHQKLVFFAEDVGSNKGAIIGLMVGGW	x	x
	1-39	DAEFRHDSGYEVHHQKLVFFAEDVGSNKGAIIGLMVGGV	x	x
	1-38	DAEFRHDSGYEVHHQKLVFFAEDVGSNKGAIIGLMVGG	x	x
	1-37	DAEFRHDSGYEVHHQKLVFFAEDVGSNKGAIIGLMVG	x	
	1-36	DAEFRHDSGYEVHHQKLVFFAEDVGSNKGAIIGLMV	x	
N-truncated A $\beta$	2-42	AEFRHDSGYEVHHQKLVFFAEDVGSNKGAIIGLMVGGWIA		x
	pE3-42	<u>E</u> FRHDSGYEVHHQKLVFFAEDVGSNKGAIIGLMVGGWIA		x
	4-42	FRHDSGYEVHHQKLVFFAEDVGSNKGAIIGLMVGGWIA		x
	8-42	SGYEVHHQKLVFFAEDVGSNKGAIIGLMVGGVIA		x
	10-42	YEVHHQKLVFFAEDVGSNKGAIIGLMVGGWIA	x	
	pE11-42	<u>E</u> VHHQKLVFFAEDVGSNKGAIIGLMVGGWIA		x
	2-40	AEFRHDSGYEVHHQKLVFFAEDVGSNKGAIIGLMVGGV	x	x
	3-40	EFRHDSGYEVHHQKLVFFAEDVGSNKGAIIGLMVGGW		x
	pE3-40	<u>E</u> FRHDSGYEVHHQKLVFFAEDVGSNKGAIIGLMVGGW	x	x
	4-40	FRHDSGYEVHHQKLVFFAEDVGSNKGAIIGLMVGGW	x	x
	5-40	RHDSGYEVHHQKLVFFAEDVGSNKGAIIGLMVGGW	x	x
	7-40	DSGYEVHHQKLVFFAEDVGSNKGAIIGLMVGGW	x	x
	8-40	SGYEVHHQKLVFFAEDVGSNKGAIIGLMVGGW	x	x
	9-40	GYEVHHQKLVFFAEDVGSNKGAIIGLMVGGW	x	x
	pE11-40	<u>E</u> VHHQKLVFFAEDVGSNKGAIIGLMVGGW		x
Bi-truncated A $\beta$	2-39	AEFRHDSGYEVHHQKLVFFAEDVGSNKGAIIGLMVGGV	x	
	2-37	AEFRHDSGYEVHHQKLVFFAEDVGSNKGAIIGLMVG	x	
	9-38	GYEVHHQKLVFFAEDVGSNKGAIIGLMVGG	x	

Underlined letter E indicates N-terminal pyroglutamate modification

in the mechanisms of A $\beta$  processing, with DS plaques shaped primarily by N-terminal modifications and sAD plaques characterized by broader truncation diversity.

#### Peptide co-localization patterns and protofibrillar A $\beta$

To further interrogate the internal organization of plaques, we performed correlation analyses between different peptide signals within individual plaques across patients (Fig. 4e). This approach allowed us to assess the degree of spatial co-occurrence among different A $\beta$  species, thereby providing insight into their aggregation relationships. The analysis revealed that different A $\beta$  species exhibited significantly stronger inter-correlations in sAD compared to DS, where these associations were notably weaker.

To contextualize these spatial relationships with the soluble A $\beta$  pool, we measured soluble aggregated A $\beta$ <sub>x-40</sub> and A $\beta$ <sub>x-42</sub> using electrochemiluminescence Meso Scale Discovery (MSD) assays. Levels of A $\beta$ <sub>40</sub>, A $\beta$ <sub>42</sub>, and A $\beta$ <sub>40/42</sub> did not differ substantially between DS and sAD, despite two outliers in each group (Supplementary Fig. 2), suggesting broadly comparable production and clearance of full-length species. Taken together, the integration of correlation analyses with protofibril measurements highlights that, despite similar soluble A $\beta$  burdens, DS and sAD diverge markedly in the structural plaque assembly.

#### Discussion

In this study, we investigated the spatial distribution, molecular composition, and aggregation patterns of A $\beta$  peptides in DS and sAD. Using a combination of fluorescence histology, a reflector-mode MALDI-MSI approach, and electrochemiluminescence-based assays, we provide new insights into the differences in plaque and tangle morphology, peptide repertoires, truncation patterns, and spatial assembly of A $\beta$  deposits between the two conditions.

Our data confirm and extend prior observations that although the abundance of A $\beta$  and tau lesions is comparable between DS and sAD, the lesions in DS are significantly larger in size [20]. The presence of larger A $\beta$  plaques and NFTs in DS suggests that A $\beta$  and tau pathologies co-occur, leading to accelerated and more severe pathology relative to sporadic disease. While previous study has noted increased plaque size in DS [20], our findings provide new evidence that NFTs are similarly affected, underscoring a coordinated amplification of A $\beta$ -tau interactions.

Beyond morphology, our plaque-resolved MALDI-MSI analysis uncovered fundamental differences in A $\beta$  peptide composition (summarized in Fig. 5). DS plaques contained a broader and more diverse repertoire of A $\beta$  species, including A $\beta$ <sub>2-42</sub>, A $\beta$ <sub>pE3-42</sub>, A $\beta$ <sub>3-40</sub>, A $\beta$ <sub>4-42</sub>, A $\beta$ <sub>8-42</sub>, A $\beta$ <sub>pE11-40/42</sub>, which were absent from sAD

	Sporadic Alzheimer's disease	Down Syndrome
Pathology	■ Aβ production	↑↑ Aβ production
	↓↓ Aβ clearance	■ Aβ clearance
Aβ N-truncations	✓	✓✓
Aβ C-truncations	✓✓	✓
Dual Aβ truncations	✓	-

**Fig. 5** Schematic overview summarizing pathological features and key findings in sporadic Alzheimer's disease and Down Syndrome

plaques. These truncated species are highly aggregation-prone and may contribute to the earlier onset and accelerated plaque development characteristic of DS. The detection of AβpE11 variants is particularly noteworthy given the overexpression of BACE2 in DS, a protease capable of generating N-terminal truncations at this position [43]. By contrast, sAD plaques displayed a narrower but chemically more heterogeneous pattern, characterized a set of unique bi-terminal truncations (i.e., Aβ2-37, Aβ2-39, Aβ9-38). The presence of these sAD-specific isoforms points to a more complex proteolytic environment, likely involving sequential action of amino- and carboxypeptidases. Interestingly, N-terminally truncated Aβ species such as pE3-42 and Aβ4-42, which have been reported as among the most abundant peptides in bulk cortical sAD samples [44], were less prominent in our MALDI-MSI analyses. In our dataset, these species were primarily detected in DS samples. This observation aligns with evidence that distinct truncated Aβ variants, including AβpE3-42, play prominent roles in human plaque pathology but may vary depending on plaque type and maturation [24], a pattern that may also be influenced by ApoE genotype, as all sAD cases in our study were ε3/ε3. Further studies, into Aβ peptide composition across ApoE genotypes, are however needed. Furthermore, these peptides are generally more abundant in bulk tissue, which integrates signals across many plaques, but also includes Aβ peptides of different aggregation state. Single-plaque MALDI-MSI captures plaque-specific signals and may therefore show comparatively lower levels. Together, these observations underscore the importance of single-plaque analyses for understanding plaque heterogeneity and suggest that some peptides abundant in bulk tissue may not be equally represented in individual plaques.

These differences became especially clear when we examined the relative amount of Aβ truncations. DS plaques were dominated by N-terminal truncations, with near-equal contributions from Aβ40- and Aβ42-derived species, suggesting a broadly acting aminopeptidase or alternative cleavage pathway. In contrast, sAD

plaques contained a disproportionate enrichment of truncated Aβ40, while Aβ42 remained largely full-length. This asymmetry may indicate preferential processing of Aβ40 in sAD, whereas DS favors a non-selective mechanism that acts on both Aβ 40- and Aβ42-mers. Such divergence underscores that Aβ pathology in DS is not simply accelerated sAD, but follows distinct processing trajectories.

Our comparison of soluble Aβ protofibrillar pools through IP-MSD provided an additional layer of information. It indicated that soluble, yet aggregated forms of Aβ do not differ between the patients. Similarly to the previous studies [12, 19], the spatial density of Aβ and tau NFT was broadly similar between DS and sAD. This suggests that, at the given stage of disease, the overall production, clearance, and deposition of these species are balanced across the diseases. In light of the MSI data, these apparently similar pools masked deeper compositional and spatial differences, suggesting that, while the initial development of Aβ pathology in sAD and DS is driven by the same aggregation mechanism, the progression and maturation of the pathology are distinct and modulated by distinct processes. In both diseases, we observed relative outliers. The highest values observed for Aβx-40 in the sAD and DS groups corresponded to female individual cases with particularly extensive Aβ pathology (sAD2 and DS2). Other female subjects in both groups exhibited lower Aβx-40 levels, suggesting that sex is unlikely to contribute to the elevated Aβ levels observed in the current cohort. Instead, it is likely that the elevated levels of Aβx-40 and the ratio Aβx-40/Aβx-42 are caused by the high content of Aβ-covered vessels in the homogenate.

It is also worth noting that samples from non-demented controls exhibit only slightly lower protofibrillar Aβ42 levels as compared to sAD and DS cases (Supplementary Fig. 2), despite the absence of visible plaques and lack of quantifiable Aβ signal in MSI (Fig. 2 and Supplementary Fig. 1). Therefore, this likely reflects the presence of soluble or oligomeric Aβ species that are not organized into detectable aggregates. LCO used in this study primarily stains β-sheet-rich, aggregated peptides, so these soluble

protofibrils would not be visualized by this dye. This observation is consistent with previous studies showing that protofibrillar A $\beta$  can exist in tissue even in the absence of overt plaque deposition [45, 46]. Alternatively, the A $\beta$  levels might come from vascular A $\beta$  deposition (although not observed in the tissues analyzed with IHC and MSI).

In this study, we analyzed A $\beta$  and NFT pathology only in patients with the APOE  $\epsilon$ 3/ $\epsilon$ 3 genotype. Although selective, this choice was based on the fact that APOE  $\epsilon$ 4 allele can directly influence the A $\beta$  and NFT deposition, potentially introducing a confounding factor in delineating the A $\beta$  processing machinery and pathology development. By limiting the cohort to  $\epsilon$ 3/ $\epsilon$ 3 individuals, we aimed to reduce variability attributable to APOE genotype and better isolate other pathological mechanisms. It should be noted that this study included a small number of participants (n=3 per group) and was conducted as a pilot investigation using rare post-mortem brain tissue from DS patients. While our results provide valuable insights into plaque- and NFT-level pathology, the limited sample size constrains statistical power and generalizability, and observed trends should therefore be interpreted with caution. Larger cohorts and independent validation will be necessary to confirm these findings and establish their broader relevance to sAD and DS neuropathology. However, our single-plaque analyses still highlight substantial heterogeneity in A $\beta$  composition both within and between individuals, as well as across disease groups, emphasizing that A $\beta$  pathology should not be viewed solely through aggregate measures or pathology scores. Instead, our data underscore the molecular complexity of plaque-associated A $\beta$  peptides and suggest that disease phenotypes are shaped not only by pathological burden but also by qualitative differences in peptide composition.

In summary, our study demonstrates that DS and sAD differ across several dimensions, including A $\beta$  plaque and NFT morphology, peptide repertoires, truncation patterns, and spatial assembly principles. Despite the small cohort size, the analyses demonstrated robust plaque-level findings across all participants, capturing variability between individual plaques and between patients, while still retaining clear differences between disease groups. DS pathology, marked by continuous APP-driven overproduction, does not appear to influence A $\beta$  protofibril balance as compared to sAD. Instead, the dominant discriminating factor is the packaging of A $\beta$  deposits and dominant generation of N-terminal rather than C-terminal truncations. By contrast, sAD is defined by the emergence of bi-terminal truncations and disproportionate processing of A $\beta$ 42. Together, these distinctions underscore that DS represents not simply an accelerated form

of sAD, but a distinct variant of A $\beta$  pathology shaped by unique genetic and proteolytic mechanisms.

### Supplementary Information

The online version contains supplementary material available at <https://doi.org/10.1186/s40478-026-02280-4>.

Supplementary material 1 (PDF)

### Acknowledgements

The authors thank the Netherlands Brain Bank, Institute for Neuroscience, Amsterdam and are indebted to the donors and their families for the brain tissue.

### Author contributions

K.M. conceptualized the study, acquired and analyzed the data, and prepared the manuscript. L.S. contributed to the conceptualization of the study, reviewed and edited the manuscript. E.G. participated in manuscript review and editing. M.J. contributed to manuscript review and editing. C.M. participated in manuscript review and editing. M.B. contributed to manuscript review and editing. G.O. participated in manuscript review and editing. L.L. contributed to manuscript review and editing. S.F. contributed to conceptualization and funding acquisition, reviewed and edited the manuscript. W.M. conceived and designed the study, acquired and analyzed the data, provided financial support, and prepared the manuscript.

### Funding

Open access funding provided by Uppsala University. W.M. is supported by the Swedish Alzheimer Foundation, the Swedish Cancer Foundation, the Jeansson Foundation, the Åke Wibergs stiftelse, the Åhlén-stiftelsen, the Science for Life Laboratory (SciLifeLab), and the Göran Gustafsson Foundation.

### Data availability

The datasets generated during the current study are available from the corresponding author upon reasonable request.

### Declarations

#### Ethics approval and consent to participate

All material has been collected from donors whose written informed consent for brain autopsy and the use of the material and clinical information for research purposed has been obtained by the NBB. The informed consent form of the NBB meets all current legal and ethical requirements for brain autopsy, tissue storage and use of tissue and clinical data for scientific research worldwide. The study followed the Helsinki Declaration and was approved by the Swedish Ethical Review Authority (2020-00527).

#### Consent for publication

All authors have approved the manuscript and agree with its submission.

#### Competing interests

K.M., L.S., E.G., M.J., C.M., M.B., G.O., L.L. and S.F. are employees and shareholders of BioArctic. L.L. is a co-founder and board member of BioArctic. W.M. serves as a consultant for BioArctic.

#### Author details

<sup>1</sup>BioArctic AB, Warfväges Väg 35, 112 51 Stockholm, Sweden

<sup>2</sup>Department of Public Health and Caring Sciences, Molecular Geriatrics, Uppsala University, 75237 Uppsala, Sweden

<sup>3</sup>Science for Life Laboratory, Uppsala University, 752 37 Uppsala, Sweden

Received: 8 December 2025 / Accepted: 16 March 2026

Published online: 02 April 2026

## References

- Blennow K, de Leon MJ, Zetterberg H (2006) Alzheimer's disease. *Lancet* 368:387–403
- Wildsmith KR, Holley M, Savage JC, Skerrett R, Landreth GE (2013) Evidence for impaired amyloid  $\beta$  clearance in Alzheimer's disease. *Alzheimers Res Ther* 5:33
- Dekker AD, Fortea J, Blesa R, De Deyn PP (2017) Cerebrospinal fluid biomarkers for Alzheimer's disease in Down syndrome. *Alzheimer's & Dementia: Diagn, Assess Disease Monit* 8:1–10
- Head E, Lott TI, Wilcock MD, Lemere AC (2015) Aging in Down syndrome and the development of Alzheimer's disease neuropathology. *Curr Alzheimer Res* 13:18–29
- Liu L, Saba A, Pascual JR, Miller MB, Hennessey EL, Lott IT et al (2024) Lecanemab and vascular-amyloid deposition in brains of people with Down syndrome. *JAMA Neurol* 81:1066
- Barroeta I, Videla L, Carmona-Iragui M, Fortea J, Rafii MS (2025) Current advances and unmet needs in Alzheimer's disease trials for individuals with Down syndrome: navigating new therapeutic frontiers *Alzheimer's & Dementia* 21
- Tolar M, Hey J, Power A, Abushakra S (2021) Neurotoxic soluble amyloid oligomers drive Alzheimer's pathogenesis and represent a clinically validated target for slowing disease progression. *Int J Mol Sci* 22:6355
- Bitan G, Kirkitadze MD, Lomakin A, Vollers SS, Benedek GB, Teplow DB (2003) Amyloid  $\beta$ -protein (A $\beta$ ) assembly: A $\beta$ 40 and A $\beta$ 42 oligomerize through distinct pathways. *Proc Natl Acad Sci U S A* 100:330–335
- Reinert J, Richard BC, Klafki HW, Friedrich B, Bayer TA, Wiltfang J et al (2016) Deposition of C-terminally truncated A $\beta$  species A $\beta$ 37 and A $\beta$ 39 in Alzheimer's disease and transgenic mouse models. *Acta Neuropathol Commun* 4:24
- Kummer MP, Heneka MT (2014) Truncated and modified amyloid-beta species. *Alzheimers Res Ther* 6:28
- Liu K, Doms RW, Lee VM-Y (2002) Glu11 Site cleavage and N-terminally truncated A $\beta$  production upon BACE overexpression. *Biochemistry* 41:3128–3136
- Gkanatsiou E, Sahlin C, Portelius E, Johannesson M, Söderberg L, Fältling J et al (2021) Characterization of monomeric and soluble aggregated A $\beta$  in Down's syndrome and Alzheimer's disease brains. *Neurosci Lett* 754:135894
- Ahmed M, Davis J, Aucoin D, Sato T, Ahuja S, Aimoto S et al (2010) Structural conversion of neurotoxic amyloid- $\beta$ 1–42 oligomers to fibrils. *Nat Struct Mol Biol* 17:561–567
- Zammit MD, Laymon CM, Betthausen TJ, Cody KA, Tudorascu DL, Minhas DS, et al (2020) Amyloid accumulation in Down syndrome measured with amyloid load. *Alzheimer's & Dementia: Diagnosis, Assess Disease Monit* 12
- Lemere CA, Blusztajn JK, Yamaguchi H, Wisniewski T, Saido TC, Selkoe DJ (1996) Sequence of deposition of heterogeneous amyloid  $\beta$ -peptides and APO E in Down syndrome: implications for initial events in amyloid plaque formation. *Neurobiol Dis* 3:16–32
- Kumar S, Lemere CA, Walter J (2020) Phosphorylated A $\beta$  peptides in human Down syndrome brain and different Alzheimer's-like mouse models. *Acta Neuropathol Commun* 8:118
- Frost JL, Le KX, Cynis H, Ekpo E, Kleinschmidt M, Palmour RM et al (2013) Pyroglutamate-3 amyloid- $\beta$  deposition in the brains of humans, non-human primates, canines, and Alzheimer disease-like transgenic mouse models. *Am J Pathol* 183:369–381
- Saido TC, Iwatsubo T, Mann DMA, Shimada H, Ihara Y, Kawashima S (1995) Dominant and differential deposition of distinct  $\beta$ -amyloid peptide species, A $\beta$ N3(pE), in senile plaques. *Neuron* 14:457–466
- Johannesson M, Sahlin C, Söderberg L, Basun H, Fältling J, Möller C et al (2021) Elevated soluble amyloid beta protofibrils in Down syndrome and Alzheimer's disease. *Mol Cell Neurosci* 114:103641
- Ichimata S, Martinez-Valbuena I, Lee S, Li J, Karakani AM, Kovacs GG (2023) Distinct molecular signatures of amyloid-beta and tau in Alzheimer's disease associated with Down syndrome. *Int J Mol Sci* 24:11596
- Rasmussen J, Mahler J, Beschorner N, Kaeser SA, Häslers LM, Baumann F et al (2017) Amyloid polymorphisms constitute distinct clouds of conformational variants in different etiological subtypes of Alzheimer's disease. *Proc Natl Acad Sci U S A* 114:13018–13023
- Michno W, Wehrli PM, Zetterberg H, Blennow K, Hanrieder J (2019) GM1 locates to mature amyloid structures implicating a prominent role for glycolipid-protein interactions in Alzheimer pathology. *Biochimica et Biophysica Acta (BBA) - Proteins and Proteomics* 1867:458–467
- Michno W, Wehrli P, Meier SR, Sehlin D, Syvänen S, Zetterberg H et al (2020) Chemical imaging of evolving amyloid plaque pathology and associated A $\beta$  peptide aggregation in a transgenic mouse model of Alzheimer's disease. *J Neurochem* 152:602–616
- Michno W, Nyström S, Wehrli P, Lashley T, Brinkmalm G, Guerard L et al (2019) Pyroglutamation of amyloid- $\beta$ x-42 (A $\beta$ x-42) followed by A $\beta$ 1–40 deposition underlies plaque polymorphism in progressing Alzheimer's disease pathology. *J Biol Chem* 294:6719–6732
- Kakuda N, Miyasaka T, Iwasaki N, Nirasawa T, Wada-Kakuda S, Takahashi-Fujigasaki J et al (2017) Distinct deposition of amyloid- $\beta$  species in brains with Alzheimer's disease pathology visualized with MALDI imaging mass spectrometry. *Acta Neuropathol Commun* 5:73
- Michno W, Wehrli PM, Koutarapu S, Marsching C, Minta K, Ge J et al (2022) Structural amyloid plaque polymorphism is associated with distinct lipid accumulations revealed by trapped ion mobility mass spectrometry imaging. *J Neurochem* 160:482–498
- Kaya I, Brinet D, Michno W, Başkurt M, Zetterberg H, Blennow K et al (2017) Novel trimodal MALDI imaging mass spectrometry (IMS3) at 10  $\mu$ m reveals spatial lipid and peptide correlates implicated in A $\beta$  plaque pathology in Alzheimer's disease. *ACS Chem Neurosci* 8:2778–27790
- Carlred L, Michno W, Kaya I, Sjövall P, Syvänen S, Hanrieder J (2016) Probing amyloid- $\beta$  pathology in transgenic Alzheimer's disease (tgArcSwe) mice using MALDI imaging mass spectrometry. *J Neurochem* 138:469–478
- Enzlein T, Lashley T, Sammour DA, Hopf C, Chávez-Gutiérrez L (2024) Integrative single-plaque analysis reveals signature A $\beta$  and lipid profiles in the Alzheimer's brain. *Anal Chem* 96:9799–9807
- Koutarapu S, Ge J, Dulewicz M, Srikrishna M, Szadziewska A, Wood J et al (2025) Chemical imaging delineates A $\beta$  plaque polymorphism across the Alzheimer's disease spectrum. *Nat Commun* 16:3889
- Holtzman DM, Herz J, Bu G (2012) Apolipoprotein E and Apolipoprotein E receptors: normal biology and roles in Alzheimer disease. *Cold Spring Harb Perspect Med* 2:a006312–a006312
- Castellano JM, Kim J, Stewart FR, Jiang H, DeMattos RB, Patterson BW, et al (2011) Human apoE isoforms differentially regulate brain amyloid- $\beta$  peptide clearance *Sci Transl Med* 3
- Koutarapu S, Ge J, Jha D, Blennow K, Zetterberg H, Lashley T et al (2023) Correlative chemical imaging identifies amyloid peptide signatures of neuritic plaques and dystrophy in human sporadic Alzheimer's disease. *Brain Connect* 13:297–306
- Åslund A, Sigurdson CJ, Klingstedt T, Grathwohl S, Bolmont T, Dickstein DL et al (2009) Novel pentameric thiophene derivatives for *in vitro* and *in vivo* optical imaging of a plethora of protein aggregates in cerebral amyloidoses. *ACS Chem Biol* 4:673–684
- Bankhead P, Loughrey MB, Fernández JA, Dombrowski Y, McArt DG, Dunne PD et al (2017) QuPath: open source software for digital pathology image analysis. *Sci Rep* 7:16878
- Qiang W, Yau W-M, Lu J-X, Collinge J, Tycko R (2017) Structural variation in amyloid- $\beta$  fibrils from Alzheimer's disease clinical subtypes. *Nature* 541:217–221
- Chung DC, Roemer S, Petrucelli L, Dickson DW (2021) Cellular and pathological heterogeneity of primary tauopathies. *Mol Neurodegener* 16:57
- Böken D, Cox D, Burke M, Lam JYL, Katsinelos T, Danial JSH, et al (2024) Single-molecule characterization and super-resolution imaging of Alzheimer's disease-relevant tau aggregates in human samples *Angewandte Chemie international edition* 63
- Adlard PA, Li Q-X, McLean C, Masters CL, Bush AI, Fodero-Tavoletti M, et al (2014) I $^2$ -amyloid in biological samples: not all A $\beta$ <sup>2</sup> detection methods are created equal. *Front Aging Neurosci* 6
- Valverde A, Dunys J, Lorivel T, Debayle D, Gay A-S, Lacas-Gervais S et al (2021) Aminopeptidase A contributes to biochemical, anatomical and cognitive defects in Alzheimer's disease (AD) mouse model and is increased at early stage in sporadic AD brain. *Acta Neuropathol* 141:823–839
- Bien J, Jefferson T, Čaušević M, Jümpertz T, Munter L, Multhaup G et al (2012) The metalloprotease meprin  $\beta$  generates amino terminal-truncated amyloid  $\beta$  peptide species. *J Biol Chem* 287:33304–33313
- Klafki H-W, Abramowski D, Swoboda R, Paganetti PA, Staufenbiel M (1996) The carboxyl termini of  $\beta$ -amyloid peptides 1–40 and 1–42 are generated by distinct  $\gamma$ -secretase activities. *J Biol Chem* 271:28655–28659
- Barbiero L, Benussi L, Ghidoni R, Alberici A, Russo C, Schettini G et al (2003) BACE-2 is overexpressed in Down's syndrome. *Exp Neurol* 182:335–345
- Portelius E, Bogdanovic N, Gustavsson MK, Volkman I, Brinkmalm G, Zetterberg H et al (2010) Mass spectrometric characterization of brain amyloid beta isoform signatures in familial and sporadic Alzheimer's disease. *Acta Neuropathol* 120:185–193

45. Thal DR, von Arnim C, Griffin WST, Yamaguchi H, Mrazek RE, Attems J et al (2013) Pathology of clinical and preclinical Alzheimer's disease. *Eur Arch Psychiatry Clin Neurosci* 263:137–145
46. Hérard A-S, Petit F, Gary C, Guillemier M, Boluda S, Garin CM et al (2020) Induction of amyloid- $\beta$  deposits from serially transmitted, histologically silent, A $\beta$  seeds issued from human brains. *Acta Neuropathol Commun* 8:205

### **Publisher's Note**

Springer Nature remains neutral with regard to jurisdictional claims in published maps and institutional affiliations.